

Numeric simulation of near-surface moisture migration and stress development in concrete exposed to fire

Gary R. Consolazio[†] and Jae H. Chung[‡]

Department of Civil & Coastal Engineering, University of Florida, P.O. Box 116580, Gainesville, FL 32611, USA
(Received May 6, 2003, Accepted September 15, 2003)

Abstract. A methodology is presented for computing stresses in structural concrete members exposed to fire. Coupled heat and moisture migration simulations are used to establish temperature, pore pressure, and liquid-saturation state variables within near-surface zones of heated concrete members. Particular attention is placed on the use of coupled heat and multiphase fluid flow simulations to study phenomena such as moisture-clogging. Once the state variables are determined, a procedure for combining the effects of thermal dilation, mechanical loads, pore pressure, and boundary conditions is proposed and demonstrated. Combined stresses are computed for varying displacement boundary conditions using data obtained from coupled heat and moisture flow simulations. These stresses are then compared to stresses computed from thermal analyses in which moisture effects are omitted. The results demonstrate that moisture migration has a significant influence on the development of thermal stresses.

Keywords: fire; pore pressure; slip-flow; relative permeability; thermal stress; effective stress.

1. Introduction

Assessing the performance of concrete members exposed to fire by applying analytical methods requires that consideration be given to the combined effects of temperature, moisture migration, and mechanical effects (e.g., loads and boundary conditions) (Gawin, *et al.* 1999). This is particularly true in cases involving the simulation of near-surface phenomena such as moisture clogging (Harmathy 1964, Chung and Consolazio 2003) and thermally induced explosive spalling. In these situations, the presence and migration of moisture in rapidly heated surface zones affect the development of temperature gradients (and therefore thermal stresses) and the development of internal pore pressures. Furthermore, numerical simulation of thermally induced moisture migration also requires consideration of phase-transition (liquid pore water transitioning to steam at elevated temperatures) and simultaneous multiphase fluid flow through the porous concrete skeleton.

The methodology proposed here accounts for temperature, moisture migration, and mechanical effects in a manner that permits the determination of combined stress states in rapidly heated concrete, and, moreover, facilitates the study of moisture migration phenomena (e.g., clogging) using numerical simulation. Stresses computed using the proposed methodology might later be merged with appropriate models of material failure to predict the onset and progression of failure (e.g.,

[†] Assistant Professor

[‡] Graduate Research Associate

spalling). Detailed treatment of this subsequent step, however, is beyond the scope of the present paper. Emphasis here is placed instead on identifying and evaluating, through numeric simulation, the phenomena that most significantly influence stress development in near-surface zones of heated concrete members, including an evaluation of boundary condition effects. Simulations are also used to quantify differences in temperature gradients and moisture migration in ordinary permeability and very-low permeability concrete members exposed to fire.

Quantifying the stress state within a heated concrete member requires both the determination of time-varying state variables (temperature, pore-pressure) within the system and an appropriate combination of thermal, pressure, and mechanical effects. In this paper, the first requirement is addressed by integrating multiphase constitutive fluid flow laws developed specifically for cementitious materials into an existing coupled heat and moisture flow simulation code. The second requirement is satisfied by merging state variable data obtained from the coupled heat and moisture flow simulations with finite element analyses so that thermally induced stresses and boundary condition effects can be studied.

2. Analysis of coupled heat and moisture flow in concrete

A key theme in this paper is that coupled heat and moisture flow analysis techniques should be used when quantifying thermodynamic state variables in concrete elements exposed to fire. When a concrete member is exposed to a sudden elevated temperature, heat flows across the member surface and raises the temperature of both the porous concrete skeleton and the internal pore moisture. Temperature gradients within the near-surface zones can be quite severe and depend both on the rate of heating as well as on moisture related factors such as initial saturation level and material permeability. Vaporization of pore moisture at elevated temperatures (i.e., phase-transition from liquid to steam) consumes heat energy that would otherwise raise the temperature of the solid skeleton, and thus serves a beneficial role. However, the vaporization process also generates significant internal pore pressures that drive multiphase moisture migration within the near-surface zones. Such migration can lead to phenomena such as clog formation and abrupt changes in relative permeability to gas phase flow. The net effect that moisture has on temperature development can only be adequately evaluated through coupled heat and moisture flow analysis in which multi-mode heat transport, multiphase moisture flow, and moisture phase-transition are included.

2.1. Governing equations of mass- and energy-balance

The balance laws used in this study treat concrete as a multiphase continuum in a manner analogous to that which would be used for a simple continuum. Global balances apply to the multiphase mixture as a whole via a volume averaging process (Lewis and Schrefler 1998). Balance equations form the framework for constructing the mathematical formulations of the governing field equations at the macroscopic level. The mass balance law for a multiphase mixture, which is treated as a collection of overlapping continua called phases, is given by:

$$\frac{\partial \rho}{\partial t} + \rho \operatorname{div} v = 0 \quad (1)$$

where ρ represents the volume-averaged mass density and each phase $\pi = s, l, g$ (s =solid skeleton, l =liquid, and g =gas) occupies a fraction of the overall mixture volume defined by a volume

fraction $\eta_\pi(x, t)$ such that $\rho = \sum_\pi \eta_\pi \rho_\pi$ with a mean velocity $v(x, t)$. In these expressions x represents a spatial position and t represents a temporal position (i.e., a point in time). The first term in Eq. (1) accounts for the accumulation of mass concentration in the fluid phases while the second term models mass transfer of the fluid phases with the mean macroscopic flow velocity.

The governing equation describing the macroscopic energy balance is given by:

$$\rho \frac{\partial E}{\partial t} + \nabla \cdot q - \sigma : \nabla v - \rho h = 0 \quad (2)$$

where the terms have the following physical interpretations: $\rho \{ \partial E / \partial t \}$ is the rate of change of internal energy; $\nabla \cdot q$ is the rate of heat flow, $-\sigma : \nabla v$ represents heating caused by compression and dissipative momentum transfer (e.g., elastic deformation); and $-\rho h$ represents heating by external supplies. However, based on the Helmholtz free energy and the Fourier laws of heat conduction, a coupled heat conduction equation that describes the energy balance in concrete can be explicitly expressed at the macroscopic level (Hsu 1986) as follows (see Chung 2003 for further details):

$$\rho C_p \frac{\partial T}{\partial t} = \nabla \cdot (k \nabla T) + Q + (\beta : \dot{\epsilon}) T \quad (3)$$

where C_p represents a volume-averaged specific heat at constant pressure; T is the absolute temperature of a representative element volume (REV) (Lewis and Schrefler 1998) of concrete; k represents a volume-averaged thermal conductivity; Q represents heat flow into the REV; and $(\beta : \dot{\epsilon}) T$ represents a volume-averaged thermo-elastic coupling factor. In Eq. (3), a strictly reversible energy balance is assumed between thermal-energy and associated mechanical strain energy.

In regard specifically to the mass- and energy-balance framework equations described above, the following assumptions are made here : 1) the concrete material can be characterized as a continuum via a volume averaging process such that all physical quantities (e.g., mechanical deformation, temperature) must follow continuous functions; 2) temperature changes due to mechanical deformation are assumed to be negligible (i.e., within the scope of conducting the heat and moisture flow analyses in this study, the quantity $(\beta : \dot{\epsilon}) T$ in Eq. (3) is neglected).

2.2. Numerical analysis of coupled heat and moisture flow

Solution of the mass- and energy-balance equations outlined above is accomplished here by making enhancements to, and use of, the TOUGH2 heat and mass transport simulation code (Pruess 1991). TOUGH2 employs the integral finite difference method to simulate coupled transport of water, air and heat through porous media. Although the code was originally developed for use in solving geothermal analysis problems, the authors of the present paper have modified it for use in analyzing the behavior of cementitious materials subjected to rapid and severe heating. In a previous study (Consolazio, *et al.* 1998), modifications were made to TOUGH2 to enable the analysis of radiant boundary heating conditions. Experimental data collected from radiant heating tests conducted on saturated mortar samples were then used to successfully validate the code modifications.

In the present study, further code enhancements have been made both to the TOUGH2 code and in the determination of appropriate flow parameters for simulating thermally driven multiphase moisture flow in heated concrete. These areas of improvement relate to the constitutive fluid flow

laws used by TOUGH2 and are discussed in the following section. First, however, we briefly discuss the governing equations that are solved by TOUGH2 to determine primary state variables: temperature, pressure, and saturation. In this description, we consider the system components water, dry air, and heat (denoted by $\gamma=1, 2,$ and 3 respectively) as being transported through or stored in the system domain U with surface area ∂U . The mass- and energy-balance equations can then be expressed in integral form as:

$$\underbrace{\frac{d}{dt} \int_U M^{(\gamma)} d\Omega}_a - \underbrace{\oint_{\partial U} F^{(\gamma)} \cdot n d\Gamma}_b - \underbrace{\int_U q^{(\gamma)} d\Omega}_c = 0 \quad (4)$$

where part- a represents the rate of change of mass accumulation for fluid components (water: $\gamma=1$, air: $\gamma=2$) or the rate of change of heat accumulation for the multiphase continuum (heat: $\gamma=3$); part- b represents the mass flux of fluid components ($\gamma=1$ or $\gamma=2$) or the heat flux ($\gamma=3$) into U through surface area ∂U ; and part- c represents the external supply.

The water component ($\gamma=1$) may be present in one of two phases (l =liquid and g =gas) while the dry air component ($\gamma=2$) only exists in the gas phase. Partially saturated moisture conditions may also be described from a strictly phase-oriented (as opposed to component-oriented) point of view in which we refer to overall phases π , where $\pi=l$ indicates the liquid water ($\gamma=1, \pi=l$) and $\pi=g$ indicates a mixture of water vapor ($\gamma=1, \pi=g$) and dry air ($\gamma=2, \pi=g$). For additional details, the reader is referred to Pruess (1991). Of interest here is the mass flux of the liquid phase ($\pi=l$), written as:

$$F_l = -k_{rl} K_l \frac{\rho_l}{\mu_l} X_l^{(1)} (\nabla P_l - \rho_l g \nabla z) \quad (5)$$

and the mass flux of the gas phase ($\pi=g$; a mixture of water vapor and dry air), written as :

$$F_g = -k_{rg} K_g \left(1 + \frac{b_{sf}}{P_g} \right) \frac{\rho_g}{\mu_g} (\nabla P_g - \rho_g g \nabla z) - \rho_g \tau D_g \text{grad} (X_g^{(2)}) \quad (6)$$

where $k_{r\pi}$ is the relative permeability of the porous medium to flow of fluid phase π ; K_π is the intrinsic permeability to phase π ; μ_π is the dynamic viscosity of phase π ; ∇P_π is the pressure gradient for phase π ; τ is the tortuosity factor; D_g is the effective dispersion-diffusion coefficient; and $X_\pi^{(\gamma)}$ represents the mass fraction of component γ in phase π . Within Eqs. (5) and (6), the ‘‘phase-interference’’ relative permeability terms k_{rl} and k_{rg} and the slip-flow constant b_{sf} have particular importance in the simulation of concrete exposed to fire. Constitutive flow laws focusing on these parameters are therefore discussed next.

2.3. Constitutive laws for moisture flow

In rapidly heated concrete, the primary mode of moisture flow is pressure-driven flow. Heat enters the concrete member by way of surface flux (e.g., surface radiation or convection), and subsequently begins elevating the temperature of the near-surface concrete through thermal conduction. Under severe heating conditions, internal temperatures will increase sufficiently to cause the pore moisture to vaporize and generate steam. Continued heating elevates the fluid temperature

and pressure, resulting in the evolution of pressure gradients that drive the flow of both gas and liquid phases. Of particular relevance in modeling this type of moisture flow are: 1) boundary heat flux; 2) conductive and convective heat transport within the porous medium; 3) phase-transition (vaporization and condensation) of pore moisture; 4) permeability of concrete to gas (air-steam mixture) flow; and 5) fluid phase interference (relative permeability). Item 1 was addressed in a previous study (Consolazio, *et al.* 1998); items 2 and 3 are computational features included in the TOUGH2 code; items 3 and 4 relate to constitutive modeling of fluid flow and are addressed next.

2.3.1. Gas phase slip-flow

Pressure driven transport conditions involving gases (e.g., an air-steam mixture) flowing through cementitious materials do not generally obey Darcy's law for laminar fluid flow (McVay and Rish 1995, Klinkenberg 1941). Rather, use of an alternative flow model that accounts for gas slippage, or the so-called "Klinkenberg effect", is preferable. In this study, Klinkenberg's model is used to compute flow rates of the gas phase (i.e., the air-steam mixture). In this model, the permeability of a porous medium to gas flow is assumed to be pressure dependent. If in Eq. (6), we recognize that for strongly pressure driven gas flow, the gravitational and dispersion-diffusion terms can be neglected, and if we further temporarily consider only single phase gas flow (with $k_{rg}=1$ and no phase interference due to the presence of a liquid phase), then Eq. (6) becomes :

$$F_g = -K_g \left(1 + \frac{b_{sf}}{P_g} \right) \frac{\rho_g}{\mu_g} (\nabla P_g) \quad (7)$$

In this expression, the intrinsic gas permeability K_g and the slip-flow constant b_{sf} are both characteristics of the porous medium under consideration. The term b_{sf}/P_g quantifies the extent to which flow through the porous medium deviates from laminar flow. If b_{sf}/P_g is small relative to unity, then the flow is approximately laminar and obeys Darcy's law; if b_{sf}/P_g is large, then gas slippage is significant and the flow rate will depend not only on the pressure gradient ∇P_g but also on the flow pressure P_g . It is worth noting that a term of the form b_{sf}/P_g does not appear in Eq. (5) because slip-flow is a dominant phenomenon only in gas phase flow.

Slip-flow effects are generally substantial in materials having low permeabilities (Klinkenberg 1941). Therefore, simulation of steam flow through heated porous materials such as concrete requires that the slip-flow contribution term b_{sf}/P_g be taken into account. Furthermore, an appropriate value of b_{sf} must also be selected for each material considered. Previous studies (e.g., Bamforth 1987) have proposed models that relate slip-flow constant b_{sf} to intrinsic gas permeability K_g for cementitious materials. For the cementitious materials considered here, b_{sf} values are determined using the model described by Chung (2003) :

$$b_{sf} = e^{(-0.581757 \ln(K_g) - 19.1213)} \quad (8)$$

where K_g has units of m^2 and b_{sf} has in units of atmospheres. This expression was developed for near surface moisture flow based on permeability test data published by Whiting (1988) and Klinkenberg (1941) and based on relationships between intrinsic gas permeability and intrinsic liquid permeability for concrete published by Dhir (1989). Emphasis here is placed not on the development of Eq. (8) but rather on evaluating the influence of slip-flow in concrete exposed to fire. For additional details regarding the process used to develop Eq. (8), see Chung (2003).

2.3.2. Phase interference

Phase-transitions (vaporization and condensation) and internal pressure development within heated concrete result in the simultaneous flow of multiple fluid phases. Permeability parameters such as K_l in Eq. (5) and $K_g(1 + (b_{sf}/P_g))$ in Eq. (6) represent the permeability of a material to either single phase liquid flow, or single phase gas flow, respectively, but do not account for the relative phase interference that occurs when multiple phases flow simultaneously. Interference effects are instead accounted for by making use of relative permeability functions $k_{rl} = fn(S_l)$ and $k_{rg} = fn(S_l)$ that modify—based on the current liquid saturation level S_l at a particular location in the domain U —the appropriate permeability parameters, thus yielding saturation-dependent effective permeabilities for each phase. Fluid phase mass flux rates are then computed using effective permeabilities $k_{rl}K_l$ and $k_{rg}K_g$ where $0 \leq k_{rl} \leq 1$ and $0 \leq k_{rg} \leq 1$. In this study, the following relative permeability functions have been employed:

$$k_{rg}(S_l) = 10^{S_l^\lambda} - 10^\lambda S_l \quad (9)$$

$$k_{rl}(S_l) = k_{rg}(1 - S_l) \quad (10)$$

where $\lambda = 0.05 - 22.5n$; n is the concrete porosity; and S_l is the degree of liquid saturation ($0 \leq S_l \leq 1$). Eqs. (9) and (10) were previously developed by the authors (Consolazio and Chung 1998) for use in modeling multiphase moisture flow through concrete. These relationships have also been shown to compare well with the work of other researchers (Jacobs 1998).

2.4. Numerical study of coupled heat and moisture flow

In cementitious materials, even a modest amount of liquid pore moisture can dramatically reduce the permeability of the material to gas phase flow thus altering moisture migration, pore pressure development, and heat transport (Harmathy 1964, Consolazio, *et al.* 1998, Jacobs 1998). In this section, coupled heat and moisture flow simulations are conducted using TOUGH2 and the constitutive relationships described above to evaluate the effect of moisture migration and slip-flow. A circular concrete column subjected to an “all-around” (axisymmetric) fire serves as the example structural element. Determination of temperature, liquid saturation, and pressure within the near-surface zones of the column is accomplished using the one-dimensional (1D) TOUGH2 model illustrated in Fig. 1. Surface heat flux due to the fire and moisture flow from the column to the surrounding atmosphere are modeled using numerical procedures previously described (Consolazio, *et al.* 1998) and therefore are not detailed here.

In order to evaluate the influence that fluid flow properties have on coupled thermal behavior, two different concrete mixtures are considered here. Material properties for both mixtures were obtained from the literature (Whiting 1988, Burg and Ost 1994) and are listed in Table 1. Slip-flow constants b_{sf} for the two mixtures have been determined using Eq. (8). Fire-exposure simulation cases discussed herein are listed in Table 2. Uniform initial conditions are assumed in each simulation: a uniform pressure of 1 atm (0.1013 MPa); a uniform temperature of 20 C; and a uniform distribution of liquid saturation.

2.4.1. Simulation of moisture clog formation

Case A represents an ordinary permeability concrete subjected to the ASTM E119 (ASTM 1995)

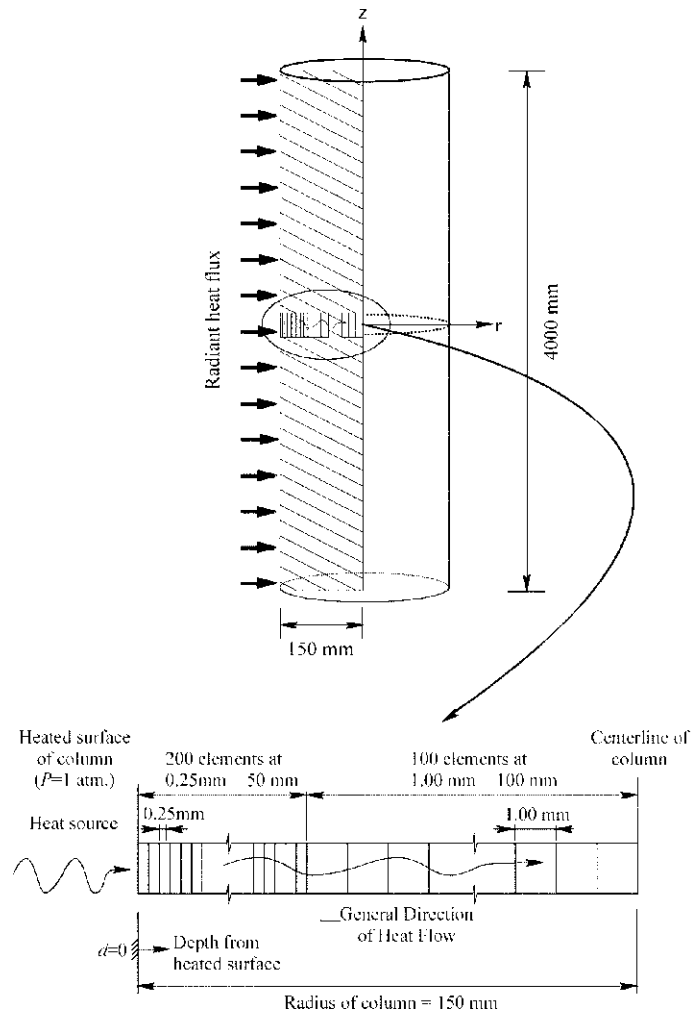


Fig. 1 Heat and moisture flow model

Table 1 Concrete material properties

Material property	Symbol	Concrete I : (Ordinary permeability)	Concrete II : (Very-low permeability)
Intrinsic gas permeability	K_g	2.24E-17 m ²	6.34E-19 m ²
Intrinsic liquid permeability	K_l	8.49E-19 m ²	4.82E-21 m ²
Slip-flow constant	b_{sf}	2.44 MPa	19.2 MPa
Porosity	n	13.3%	8.2%
Dry conductivity	κ_{dry}	1.7 W/m-C	2.0 W/m-C
Wet conductivity	κ_{wet}	2.9 W/m-C	2.6 W/m-C
Emissivity	ϵ	0.8	0.88
Specific heat	C_p	921.1 J/kg-C	921.1 J/kg-C

Table 2 Fire exposure conditions simulated

Case	Concrete	Slip-flow	Initial liquid saturation	Comments
A	I	Included	$S_l=0.4$	Baseline concrete I case (r.h.=60–65%)
B	II	Included	$S_l=0.5$	Baseline concrete II case (r.h.=60–65%)
C	II	Excluded	$S_l=0.5$	Concrete II without slip-flow
D	II	N/A	$S_l=0.0$	Concrete II without moisture effects

fire heating curve. Initial liquid saturation in the material is $S_l=0.4$, a typical equilibrium moisture content for this type of material in an environment having a relative humidity of r.h.=60–65% (Baroghel-Bouny and Chaussadent 1996). Results obtained by simulating coupled heat and moisture flow for this case are presented in Fig. 2. The plots illustrate the time-varying evolution of temperature, liquid saturation, and pore pressure within the 80 mm depth of concrete closest to the heated surface of the column. Each line running parallel to the “distance from heated surface” axis in Fig. 2 represents the system state a particular instant of time.

At time $t=0$ sec., temperature, pressure, and liquid saturation are uniform throughout the entire 80 mm depth. A short time later, the heated surface dries to a completely desaturated state and the liquid saturation abruptly drops from $S_l=0.4$ to $S_l=0.0$. As heating continues, liquid pore moisture

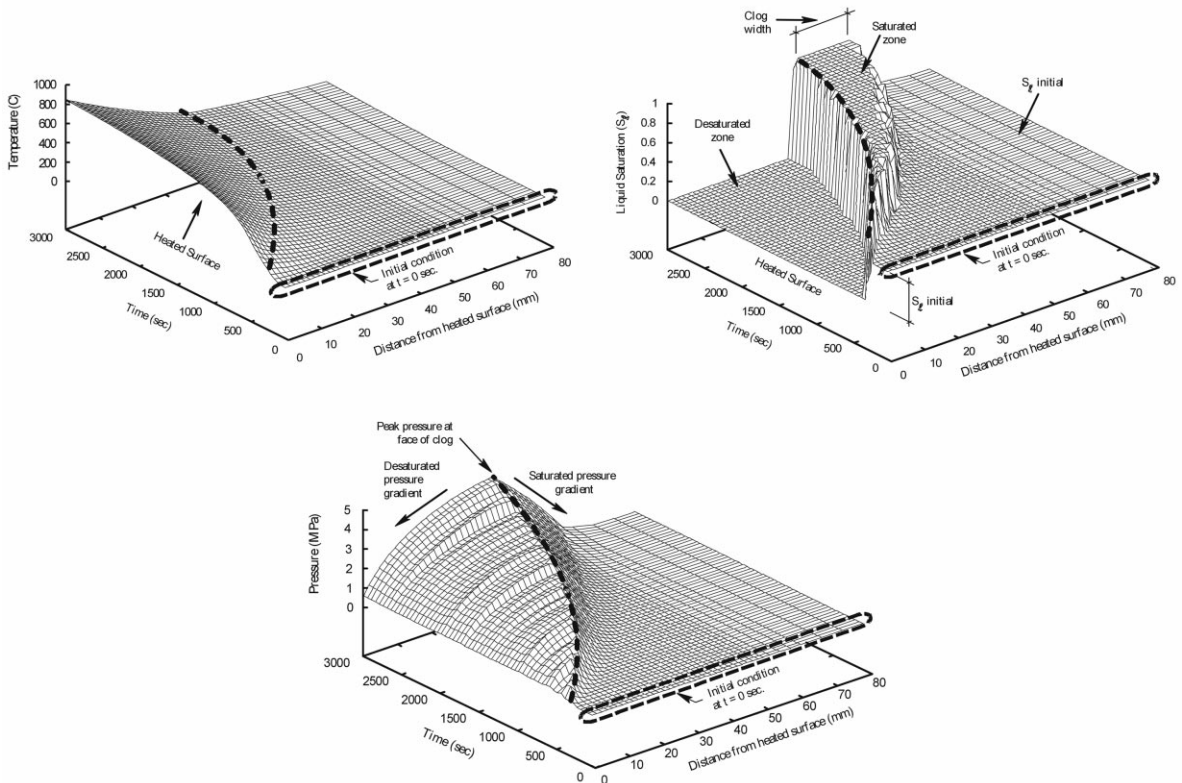


Fig. 2 Evolution of state variables in heated concrete

near the surface increases in temperature, undergoes a phase-transition to steam, and then continues to increase in temperature and pressure. The increase in internal pore pressures gives rise to pressure gradients inside the material. As Fig. 2 illustrates, pore pressure maximizes at the interface between the desaturated and saturated zones. Gas-phase moisture, migrating along the desaturated pressure gradient, escapes from the concrete into the atmosphere. In contrast, moisture moving in the opposite direction condenses in the lower temperature interior zone and adds to the liquid pore water already present at that location.

As this process continues, the degree of liquid saturation continues to increase until a fully saturated condition ($S_l=1.0$) occurs and a narrow moisture clog forms. The saturated clog creates an impermeable barrier through which gas cannot flow (i.e., the relative permeability to gas flow is $k_{rg}=0$). As a result, steam generated at the saturated front is inhibited from flowing deeper into the column and must instead migrate back to the surface to escape into the atmosphere. Continued heating results in further increases in temperature, pressure, and the thickness of the clog (as liquid in the saturated clog is forced deeper into the member by the increasing internal pressure).

The temperature gradient in the desaturated zone adjacent to the surface is more severe than the temperature gradient within or behind the clog. Heat energy flowing into the clog is partially consumed by the process of liquid pore moisture undergoing phase-transition to steam, thus the temperature increase in this area is attenuated. In contrast, heat flowing through the desaturated zone results in rapid temperature increase and a steeper thermal gradient. It is clear from the results shown that significant coupling exists between heat and moisture flow in concrete exposed to fire, and therefore, temperature and pressure data for such conditions should be computed using a coupled analysis technique.

2.4.2. Comparison of ordinary and very-low permeability materials

In order to facilitate quantitative comparison of simulation results, throughout the remainder of this paper profiles of data are given at only two instants in time: $t=300$ sec (5 mins), and $t=600$ sec. (10 mins.). In Fig. 3, profiles of temperature and internal pore pressure are presented for columns made of concrete I (case A) and concrete II (case B), each subjected to an ASTM E119 heating

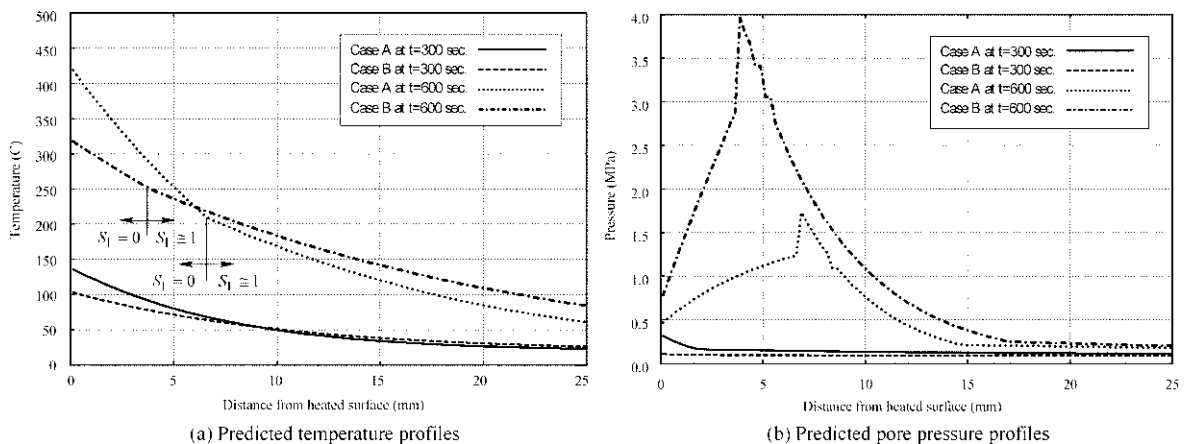


Fig. 3 Comparison of ordinary permeability and very-low permeability concrete

curve. Two differences are clearly evident: 1) the temperature gradients are noticeably different, and 2) the magnitudes of the internal pore pressures are quite different.

Due to the greater permeability of concrete I, moisture movement during heating is more prevalent in this case than in concrete II. In Fig. 3(a), the locations of moisture clogs (transition points between $S_l = 0$ and $S_l \cong 1$) at $t=600$ sec. are indicated for both cases. A steeper temperature gradient is developed in the ordinary permeability concrete due to the greater ease with which moisture can migrate (and therefore more rapidly form a desaturated zone) and due to the lower initial liquid saturation level (initial $S_l=0.4$ for concrete I and $S_l=0.5$ for concrete II). The dramatically lower gas permeability and higher initial liquid saturation of concrete II result in the formation of a moisture clog at a shallower depth from the heated surface. In addition, the lower gas permeability offers more resistance to pressure driven steam flow occurring between the clog and the heated surface and thereby generates significantly higher internal pore pressures (Fig. 3(b)). These results demonstrate that coupling between the heat and moisture flow influences not only temperature development but also internal pore pressure development.

2.4.3. Influence of slip-flow

To demonstrate the importance of accounting for gas-phase slip-flow, Fig. 4 presents results obtained from simulations in which slip-flow effects are included (case B) and excluded (case C) for concrete II. The term $K_g(1 + (b_{sf}/P_g))$ in Eq. (6) is the gas permeability of the porous medium at flow pressure P_g and is used—in conjunction with k_{rg} —to determine gas-phase mass flow rates. For concrete II, b_{sf} (Table 1) is substantial relative to the flow pressures developed (Fig. 4(b)), therefore $K_g(1 + (b_{sf}/P_g)) > K_g$. As such, when slip-flow is included in the simulation process, predicted internal pore pressures are smaller because the concrete is more permeable to gas phase flow. Omitting slip-flow effects (case C) results in significantly exaggerated predictions of internal pore pressure (Fig. 4(b)). In contrast to Fig. 3(a), where dramatic differences in the permeabilities of cases A and B resulted in significant differences in temperature profiles, few difference are noted in Fig. 4(a). This is attributable to the more modest differences in permeabilities between cases B and C that result from including and excluding the b_{sf}/P_g term.

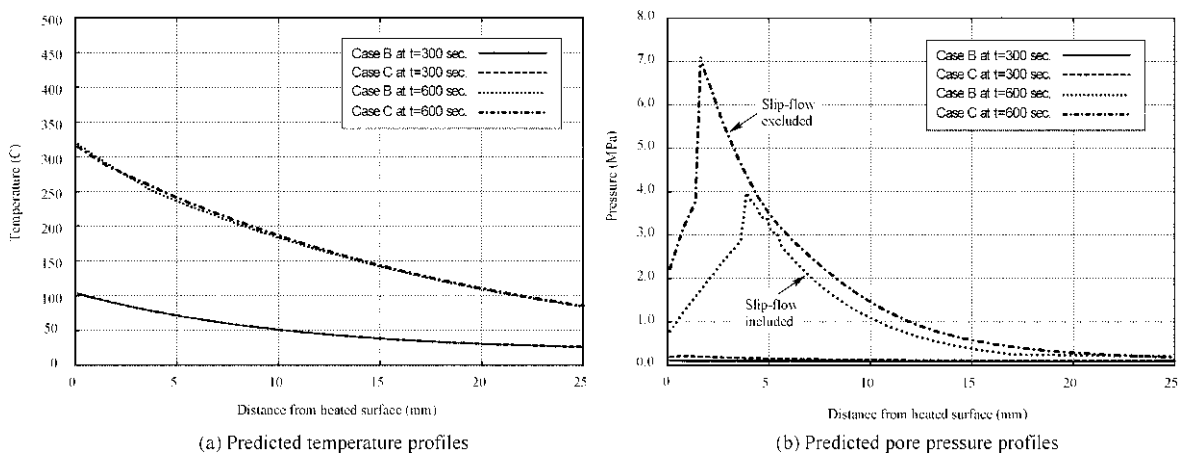


Fig. 4 Effect of including versus excluding slip-flow

3. Coupled thermo-elastic stress analysis

Having established temperature and pore pressure data using a method that accounts for coupled thermal-moisture effects, attention is now given to the computation of combined material stresses that include the effects of thermal dilatation, mechanical loading, boundary conditions, and pore pressure.

3.1. Superposition of stress and pore pressure

The discussion of stress states given here in regard to heated concrete shall be made at the macroscopic level where continuous distributions of the phases ($\pi=s, l, g$: solid, liquid, and gas respectively) are assumed. This means that at each location x within the domain U , all of the phases are present at the same time and in proportion to their volume fractions η_π . Total stress at the macroscopic level, denoted $\underline{\underline{\sigma}}$, is defined as the sum of volume-averaged quantities of stress corresponding to each phase (solid, liquid, gas). Also, continuity of the stress field across the solid-fluid interface is assumed to be valid so that the linear momentum balance equation for concrete as a multiphase continuum can be obtained. The total stress tensor $\underline{\underline{\sigma}}$ can be written in decomposed form as a combination of solid and fluid terms (Chung 2003):

$$\underline{\underline{\sigma}} = (1 - n)\underline{\underline{\sigma}}_s + n(S_l\underline{\underline{\sigma}}_l + S_g\underline{\underline{\sigma}}_g) \quad (11)$$

where n is the macroscopic porosity; $\underline{\underline{\sigma}}_\pi$ are the microscopic stress tensors for each phase; S_l is the liquid saturation; and $S_g = 1 - S_l$ is the gas saturation. If shear stresses in the liquid and gas phases are assumed to be negligible, then $\underline{\underline{\sigma}}_l$ and $\underline{\underline{\sigma}}_g$ can be written in terms of the fluid phase hydrodynamic pressures P_l and P_g and we then have :

$$\underline{\underline{\sigma}} = (1 - n)\underline{\underline{\sigma}}_s - n(S_l P_l \underline{\underline{I}} + S_g P_g \underline{\underline{I}}) \quad (12)$$

Assuming that local thermodynamic equilibrium exists, then $P_l = P_g = P$ where P is the internal pore pressure (the same quantity obtained from TOUGH2 analyses). For this condition, $(S_l P_l \underline{\underline{I}} + S_g P_g \underline{\underline{I}})$ becomes $(S_l + S_g) P \underline{\underline{I}} = P \underline{\underline{I}}$ because $S_l + S_g = 1$ and Eq. (12) may then be rewritten as:

$$\underline{\underline{\sigma}} = (1 - n)\underline{\underline{\sigma}}_s - n P \underline{\underline{I}} \quad (13)$$

Solving for the term $(1 - n)\underline{\underline{\sigma}}_s$ and denoting it $\underline{\underline{\sigma}}_s'$, we have :

$$\underline{\underline{\sigma}}_s' = \underline{\underline{\sigma}} + n P \underline{\underline{I}} \quad (14)$$

where $\underline{\underline{\sigma}}_s'$ is the effective stress acting on the solid skeleton. The quantity $\underline{\underline{\sigma}}_s'$ represents the stress carried solely by the solid skeleton and therefore may be used in assessing the potential for fracture related material failure. However, in evaluating effective stress, alternative porosity parameters may be used to more accurately reflect the failure surface involved. Bažant and Kaplan (1996) note that boundary porosity, n_p , may be more appropriate in computing effective stresses in concrete. They define n_p as the porosity of the “macroscopically planar but microscopically tortuous weakest

section through the material” and note that $n_p \cong 0.9$ is a reasonably representative value for concrete. Thus, in the present study, effective stresses are computed as :

$$\underline{\sigma}'_s = \underline{\sigma} + n_p P \underline{I} \quad (15)$$

where $n_p=0.9$ is used throughout.

3.2. Finite element thermo-elastic stress analysis

Computation of effective stresses using the method described above requires that pore pressures be combined with stresses that are induced by thermal dilation, mechanical load, and boundary condition restraint. Here, finite element based thermo-mechanical analysis –using the ADINA finite element code (ADINA 2002)– is used for the purpose of computing these thermal stresses. Linear elastic axisymmetric finite element models (Fig. 5) are used to analyze the circular concrete column introduced earlier (Fig. 1). Since the degree of restraint provided by the column boundaries will affect the thermal-dilation related stresses that are computed, we consider here two different sets of boundary conditions that bracket realistic field conditions. In the first case (Fig. 5(b)), vertical and radial expansion are completely restrained, while in the second (Fig. 5(c)), the top of the column is free to expand.

The thermo-mechanical stress analyses conducted here are considered to be one-directionally coupled because, as was noted earlier, temperature changes are assumed to induce thermal-dilational deformation but mechanical deformations are assumed to produce no change in system temperature. This assumption permits us to compute the time-varying temperature field separately, and then to apply

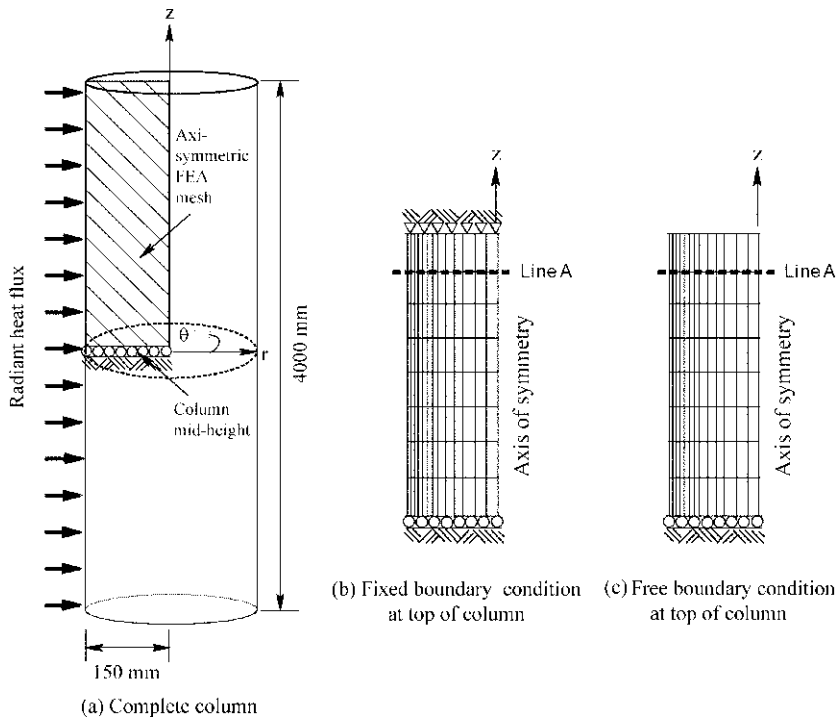


Fig. 5 Axisymmetric finite element models of concrete column

that temperature field to finite element thermal stress models to evaluate time-varying thermal stresses.

Using TOUGH2 to solve the coupled heat and moisture flow equations yields a complete time-varying description of the temperature field throughout radial direction of the column (recall that the one-dimensional TOUGH2 model represents a typical radial slice of the example circular column, as is illustrated in Fig. 1). Temperature data from the one-dimensional TOUGH2 models is then mapped onto nodes located along radial lines in the axisymmetric finite element thermal stress models (Fig. 5). For each finite element model nodal point, a complete time-history of temperature is extracted from the TOUGH2 simulation results and is then applied to the finite element model as a time-varying prescribed nodal temperature. Time-varying thermal stress analyses are then performed for each boundary condition model to compute time-histories of thermal stresses throughout the two-dimensional axisymmetric meshes.

To enhance the clarity of the example cases presented below, the effects of mechanical loads such as axial column forces and flexural moments have been omitted. Focus is placed instead on the effect that restraint of thermal expansion has on stress development. However, the stress superposition methodology described above and employed in the examples below is also directly applicable, without any need of modification, to the analysis of situations involving mechanical loads.

3.3. Combined stress results

Evaluating combined stress effects is accomplished here by computing effective stresses in accordance with Eq. (15). In this context, the thermal stresses computed by finite element analysis are taken as $\bar{\sigma}$ since they represent the macroscopically averaged effect of thermal dilation. Eq. (15) is then used to combine thermal stresses with separately computed pore pressures so that effective stresses may be determined.

Of interest here are both the magnitudes of principal stresses developed and the differences in stress predictions that arise from different treatments of moisture effects. In Figs. 6 and 7, maximum and minimum principal effective stresses along line-A (Fig. 5) are presented at $t=600$ sec. (10 mins.) for the free and fixed thermal restraint boundary conditions. Results for case B are plotted twice—once with both thermal stresses and pore pressure effects included; and once with only thermal stresses included (i.e., pore pressure effects excluded). In this manner, an assessment of the relative contributions of thermal stress and pore pressure can be made. In addition, thermal stresses computed for case D—a heat flow analysis in which moisture effects have been completely excluded from the determination of temperature data - are also shown.

Figs. 6 and 7 indicate that stress data computed with consideration of moisture effects (case B) are generally much less severe than corresponding data computed without consideration of moisture effects (case D). Phase-transition and migration of moisture during exposure to fire reduce the severity of thermal gradients developed and thus reduce the severity of thermal stresses.

In regard to Fig. 6(a) (fixed boundary condition), very large principal tensile stresses are developed in the radial direction of the near-surface zone. In fact, the stresses computed here would exceed the tensile strength of the concrete if the strength decrease at elevated temperatures had been considered in the constitutive model (such treatment is beyond the scope of the linear elastic material model employed here). Even in the free boundary condition case (Fig. 6(b)), tensile stresses within the first 10 mm of depth are in the range of typical concrete tensile strength at elevated temperatures (Nechnech, *et al.* 2002). The effect of pore pressure in the near surface zone is also evident in Fig. 6(b). At approximately 4 mm of depth, the peak in the pore pressure profile (see

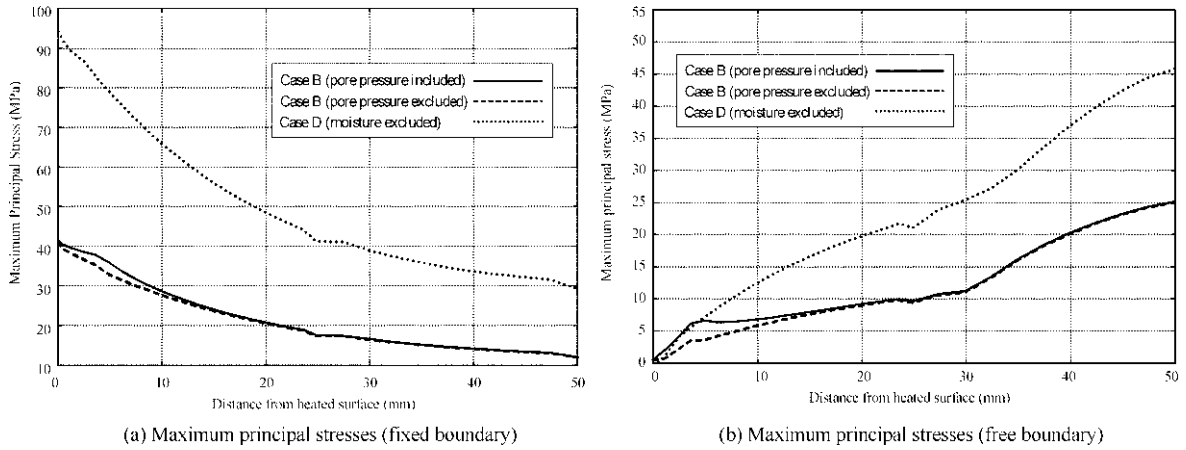


Fig. 6 Comparison of maximum principal stresses at $t=600$ sec

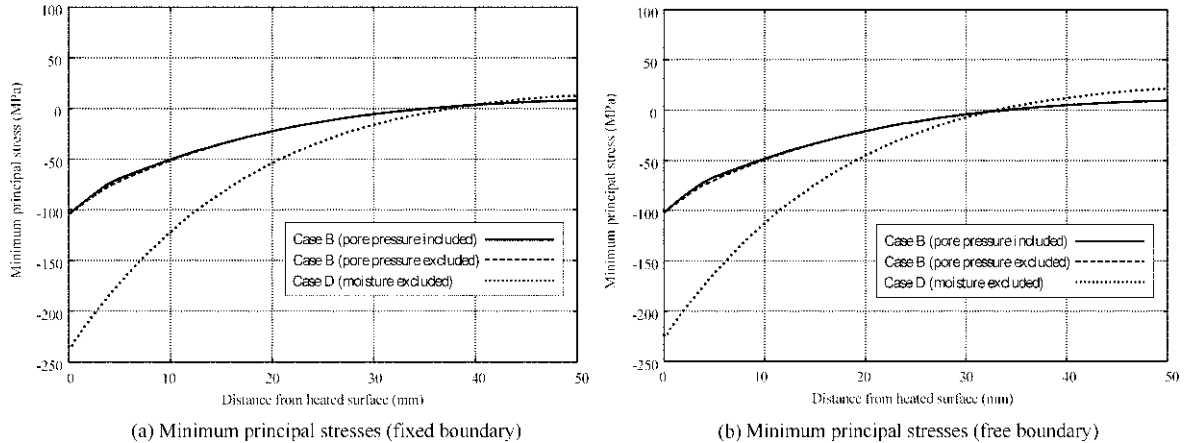


Fig. 7 Comparison of minimum principal stresses at $t=600$ sec

also Fig. 3(b), case B, $t=600$ sec.) adds a significant contribution to the baseline thermal stress (i.e., Fig. 6(b), case B with pore pressure excluded). Thus, while the contributions of pore pressure are nearly negligible in the fixed boundary case (Fig. 6(a)) they are not in the free boundary case (Fig. 6(b)). The latter boundary condition would be typical of zones not immediately adjacent to the top or bottom of a column.

Finally, it is noteworthy that significant compressive stresses are developed in both boundary condition cases (Fig. 7). Large compressive hoop-stresses in the θ -direction of the model are developed as the outer shell of the column attempts to thermally dilate but is restrained by the cooler inner core. In regard to these compressive stresses, pore pressure effects are found to be negligible (Fig. 7).

4. Applications of the proposed methodology

Several areas of potential application exist with respect to the numerical methodology proposed

here. The effects of intensity and duration of thermal loading, member cross-sectional geometry, layout of reinforcing steel, and concrete cover thickness may all be evaluated using the proposed methodology. For example, Chung (2003) developed detailed three-dimensional models of a square cross-section reinforced concrete column. By modeling the reinforcing steel separately from the surrounding concrete, and then using the stress computation methodology proposed in this paper, thermally induced stresses near the heated surfaces of the column were numerically quantified. Results obtained by Chung indicate that definite linkages exist between structural design parameters (concrete cover thickness, member cross-sectional shape, and reinforcing layout) and material response parameters (moisture level, pore pressure, thermal gradient, and ultimately stress). Development of design guidelines aimed at improving the performance of concrete elements exposed to fire will benefit directly from the results of numerical studies of this form and from the stress prediction methodology proposed in the present paper.

In addition, future efforts should also focus on the development of temperature dependent material failure models for reinforced concrete. Combining such models with the stress prediction methodology proposed herein will facilitate direct comparisons between numerically predicted structural performance data and corresponding data obtained from experimental test programs involving exposure of concrete elements to severe thermal loading conditions (e.g., Phan, *et al.* 2001, Kodur 1998, Kodur and Lie 1997).

5. Conclusions

A numerical methodology for simulating near-surface heat and moisture migration in concrete exposed to fire has been presented. Constitutive fluid flow laws applicable to pressure-driven gas and liquid phase moisture flow through concrete have been used to numerically predict the formation and evolution of moisture clogs. Results obtained from coupled heat and moisture flow simulations have demonstrated that both migration and phase-transition of moisture alter the temperature gradients that develop in near-surface zones of concrete elements exposed to fire. Simulations have also predicted the development of large internal pore pressures during heating, especially in very-low permeability concrete.

A superposition procedure for combining stresses due to mechanical loads and thermal dilation together with internal pore pressures is presented and used to compute effective stresses in circular concrete columns exposed to fire. It has been found that thermal stresses differ significantly between cases in which moisture effects have been included and excluded from the process of determining temperature data. Stress contributions due to internal pore pressure development during heating have been approximately quantified and have been found to be non-negligible, but of lesser magnitude than thermal stresses.

Acknowledgements

The authors wish to acknowledge the financial support of the National Science Foundation under Grant No. CMS-9900015.

References

ADINA (2002), ADINA Research and Development Inc. *ADINA Theory and Modeling Guide*. Report ARD

- 02-7, Watertown, MA.
- ASTM (1995), ASTM E 119-95a, "Standard test methods for fire tests of building construction and materials", *Annual Book of ASTM Standards*, 1995, American Society for Testing and Materials (ASTM), West Conshohocken, PA, 441-461.
- Bamforth, P.B. (1987), "The relationship between permeability coefficients for concrete obtained using liquid and gas", *Mag. Concr. Res.*, **30**(138), 233-241.
- Baroghel-Bouny, V. and Chaussadent, T. (1996), "Texture and moisture characterization of hardened cement pastes and concrete from water vapor sorption measurements", *The Modeling of Microstructure and Its Potential for Studying Transport Properties and Durability*, Nato ASI Series (304), Kluwer Academic Publishers, Boston, MA, 241-255.
- Bazant, Z.P. and Kaplan, M.F. (1996), *Concrete at High Temperatures : Material properties and mathematical modeling*, Longman Group Limited, Essex, England.
- Burg, R.G. and Ost, B.W. (1994), *Engineering Properties of Commercially Available High Strength Concretes*, PCA Research and Development Bulletin RD104T, Skokie, IL.
- Chung, J.H. (2003), "Numerical simulation of hygro-thermo-mechanical behavior of concrete structures exposed to elevated temperatures", Doctoral Dissertation, Department of Civil & Coastal Engineering, University of Florida.
- Chung, J.H. and Consolazio, G.R. (2003), "Moisture movement and heat flow in reinforced concrete columns subjected to fire", *Proceedings of the Second MIT Conference on Computational Fluid and Solid Mechanics*, Boston, MA, **2**, 1287-1292.
- Consolazio, G.R., McVay, M.C. and Rish, J.W. III (1998), "Measurement and prediction of pore pressures in saturated cement mortar subjected to radiant heating", *ACI Mater. J.*, **95**(5), 525-536.
- Consolazio, G.R. and Chung, J.H. (1998), "Numerical prediction of pore pressure in concrete structures subjected to rapid heating", *Proceedings of the Fifth International Conference on Composites in Engineering: ICCE/5*, Las Vegas, NV, USA, July.
- Dhir, R.K., Hewlett, P.C. and Chan, Y.N. (1989), "Near surface characteristics of concrete: Intrinsic permeability", *Mag. Concr. Res.*, **41**(147), 87-97.
- Gawin, D., Majorana, C.E. and Schrefler, B.A. (1999), "Numerical analysis of hygro-thermal behavior and damage of concrete at high temperature", *Mech. Cohes.-Frict. Mater.*, **4**, 37-74.
- Harmathy, T.Z. (1964), "Effect of moisture on the fire endurance of building elements", *Moisture in Materials in Relation to Fire Tests*, ASTM Publication STP 385, American Society of Testing and Materials, 74-95.
- Hsu, T. (1986), *The Finite Element Method in Thermomechanics*, Allen & Unwin, Inc., London, UK.
- Jacobs, F. (1998), "Permeability to gas of partially saturated concrete", *Mag. Concr. Res.*, **50**(2), 115-121.
- Klinkenberg, L.J. (1941), "The permeability of porous media to liquids and gases", *API Drilling and Production Practice*, American Petroleum Institute, 200-207.
- Kodur, V.K.R. and Lie, T.T. (1997), "Evaluation of fire resistance of rectangular steel columns filled with fibre-reinforced concrete", *Can. J. Civ. Eng.*, **25**, 339-349.
- Kodur, V.K.R. (1998), "Performance of high strength concrete-filled steel columns exposed to fire", *Can. J. Civ. Eng.*, **25**, 975-981.
- Lewis, R.W. and Schrefler, B.A. (1998), *The Finite Element Method in the Static and Dynamic Deformation and Consolidation of Porous Media*, John Wiley & Sons, Inc., New York.
- McVay, M.C. and Rish, J.W. III (1995), "Flow of nitrogen and superheated steam through cement mortar", *J. ThermoPhysics Heat Transfer*, **9**(4), 790-792.
- Nechnech, W., Meftah, F. and Reynouard, J.M. (2002), "An elasto-plastic model for plain concrete subjected to high temperatures", *Eng. Structures.*, **24**, 597-611.
- Phan, L.T., Lawson, J.R. and Davis, F.L. (2001), "Effects of elevated temperature exposure on heating characteristics, spalling, and residual properties of high performance concrete", *Materials and Structures*, **34**, 83-91.
- Pruess, K. (1991), *TOUGH2 : A General-Purpose Numerical Simulator for Multiphase Fluid and Heat Flow*, Earth Sciences Division, Lawrence Berkeley Laboratory, University of California, Berkeley, CA 94720, Document LBL-29400.
- Whiting, D. (1988), "Permeability of selected concrete", *Permeability of Concrete*, ACI Publication SP-108, American Concrete Institute, 195-222.